2

Methods

The first chapter of this thesis describes our current understanding of the physical and chemical processes active in pre- and proto-stellar environments, which set the initial conditions for the formation of low-mass stars. This chapter dives into the observational methods at the foundation of the present-day picture of the evolution of protostars: astronomical observations of interstellar molecules.

Astronomical observations are the only tools available to directly access the chemistry at play in regions of ongoing star and planet formation. This is because the closest stellar nurseries to the Solar System are situated at best ~100 pc away, thus physically unreachable by current space missions. Observations can be conducted with ground-based telescopes, at well-designated spectral ranges where the Earth's atmosphere is transparent enough. Alternatively, space-based telescopes are used to observe molecules at wavelengths at which Earth's atmosphere is opaque.

A major limitation of astronomical observations is the lack of emissivity of the most abundant interstellar molecule, molecular hydrogen (H_2), at the typical densities and temperatures of stellar and planet formation. Fortunately, spectral features of more than two hundred interstellar species are detectable beyond H_2 (McGuire, 2018), which are excellent diagnostics of the physical and chemical conditions of the earliest stellar stages (Herbst and van Dishoeck, 2009). Strictly speaking, observations of molecular species are feasible at all frequencies from ultraviolet (UV) to radio wavelengths. Practically, most of the observations of molecular species are conducted at infrared (IR), sub-millimeter and millimeter wavelengths.

2.1 MOLECULAR SPECTROSCOPY

Molecular emission and absorption recorded during observational runs can be used as probes of the physico-chemical conditions of a wide range of astronomical objects (Herbst and van Dishoeck, 2009; Jørgensen *et al.*, 2020). This section provides a summary overview of molecular spectroscopy and of the transitions assigned to molecular species in pre- and proto-stellar environments.

Compared to atoms, whose spectra consists of mere electronic transitions, molecules possess further degrees of freedom associated with the rotation and vibration of their atoms. This implies that each molecular electronic
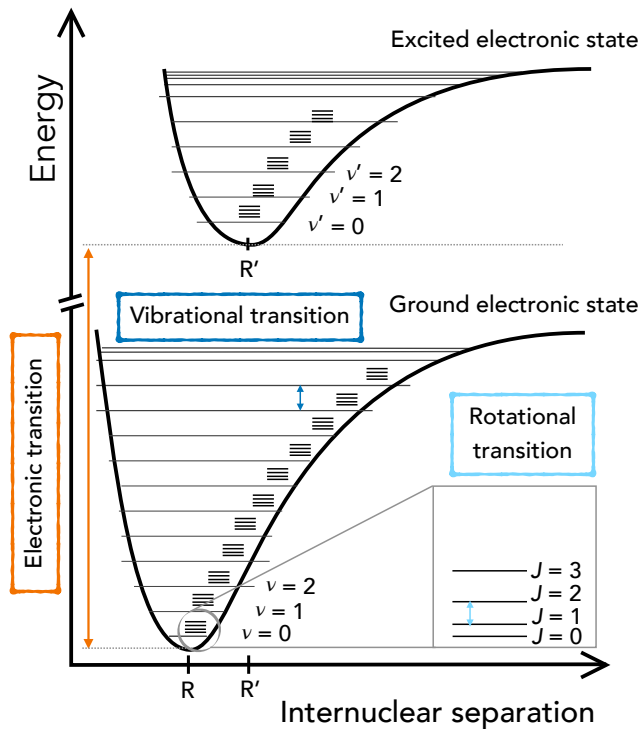
FIGURE 2.1: The electronic, vibrational, and rotational levels of a diatomic molecule. Electronic transitions arise between discrete vibrational and rotational levels in each electronic state.

state is accompanied by a suite of vibrational energy levels. And, in turn, to each vibrational level correspond a set of rotational levels (Figure 2.1). Therefore, the total energy E of a molecule can be described as the sum of its electronic E_{el}, vibrational E_{vib} and rotational E_{rot} energies:

$$E = E_{el} + E_{vib} + E_{rot}. \tag{2.1}$$

Molecules undergo rotational, vibrational and electronic transitions, by populating their energy levels upon absorption and emission of photons at discrete energies, i.e. *quanta* (Planck, 1900). For instance, a diatomic linear molecule, e.g. CO, can be considered as a rigid rotor. In this approximation, the energy needed to populate its rotational levels is equal to:

$$E_{rot} = \frac{\hbar^2}{2I} J(J+1) \tag{2.2}$$

where $\hbar$ is the reduced Planck constant, I is the moment of inertia and J is the rotational quantum number. Relatively low energies are required to populate the rotational levels of molecules akin to CO, which correspond to pure rotational transitions at far-infrared, submillimeter and millimeter wavelengths (Sect. 2.3).

Higher energies are needed to populate vibrational levels, which are associated with transitions in the infrared range of the electromagnetic spectrum (Sect. 2.2). In the harmonic oscillator approximation, the vibrational energy of a molecule is defined as:

$$E_{vib} = 2\pi \nu_0 \hbar (\nu + \frac{1}{2}) \tag{2.3}$$

where ν_0 is the natural frequency of the oscillation and ν is the vibrational quantum number. The vibrational energy is related to the oscillation of the bonds within a molecule, which are referred to as *vibrational modes*. The most common modes are *stretching* and *bending*, during which vibrations change the bond length and the bond angle, respectively. Besides hosting pure vibrational transitions, the infrared spectral range is where *ro-vibrational* transitions arise, which involve simultaneous transitions between rotational and vibrational levels.

Finally, even higher energies are required for electronic transitions to occur. These often lie in the ultraviolet-visible spectral domains and reflect the promotion of an electron to an higher energy orbital within the same molecule. The electron promotion normally takes place from the highest occupied molecular orbital (HOMO) to the lowest unoccupied molecular orbital (LUMO), following an energetically favourable transition.

The following sections describe how observations of molecular species at infrared wavelengths are carried out. Particular focus is given to the observations of solid-state molecules in absorption and to the spectral decomposition method used in this thesis to study the molecules residing on the ice mantles in the coldest regions of protostellar envelopes.

2.2   OBSERVING MOLECULES AT INFRARED WAVELENGTHS

Molecular vibrations give rise to spectral features in the near- ($0.7 - 5\ \mu$m), mid- ($5 - 30\ \mu$m) and far-infrared ($30 - 300\ \mu$m), which are used to explore the gas-phase and solid-state compositions in a variety of astronomical environments (e.g., van Dishoeck and Blake, 1998; Pontoppidan *et al.*, 2014; Boogert *et al.*, 2015). Most infrared gas-phase compositional studies are carried out in emission and probe warm gas, e.g., in the inner disks (Pontoppidan *et al.*, 2019). In contrast, solid-state molecules are predominantly studied in absorption, which allows to trace the constituents of ice mantles before their sublimation (Boogert *et al.*, 2015).

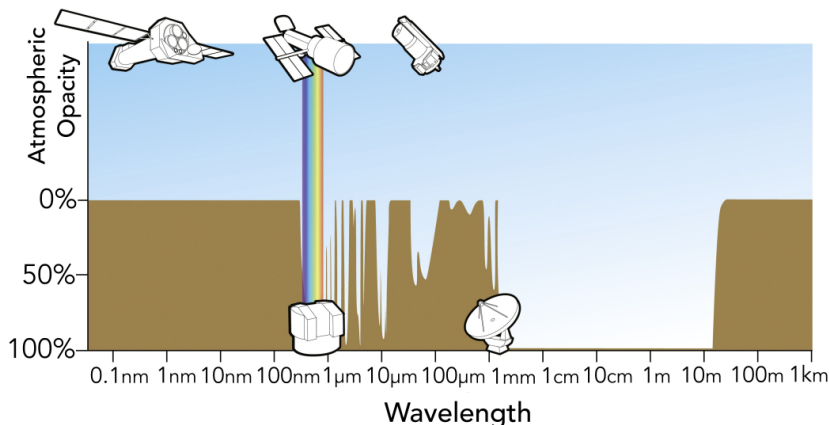Infrared observations are performed both from the ground and from

FIGURE 2.2: Electromagnetic transmittance or opacity of the Earth's atmosphere as function of wavelength. Only in a few infrared-wavelength ranges Earth's atmosphere is sufficiently transparent to carry out infrared ground-based observations. Ground-based observations are possible in the radio atmospheric window. Credit: ESA/Hubble/F. Granato.
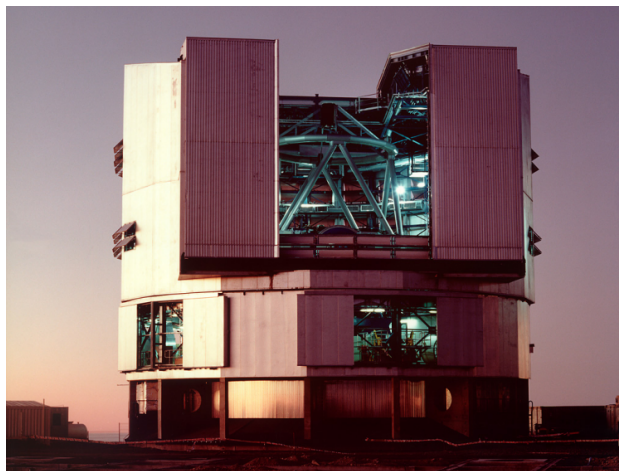
FIGURE 2.3: The ANTU telescope unit of the Very Large Telescope (VLT) - Cerro Paranal, Chile. Credit: ESO.

space, albeit the coverage of the entire infrared spectral domain ($\approx 0.7 - 300$ μm) is exclusively achievable from space. Figure 2.2 illustrates this, by displaying the electromagnetic transmittance or opacity of the Earth's atmosphere as function of wavelength. It can be noted that the majority of the infrared light proceeding from space is absorbed by Earth's atmospheric gases, mainly water vapour and carbon dioxide. Only in a few infrared-wavelength ranges Earth's atmosphere is not opaque and hence the infrared light can be observed with ground-based infrared facilities. Besides telluric absorption, a second obstacle to the feasibility of infrared ground-based observations is the emission of the Earth's atmosphere itself, which radiates at ~ 10 μm, challenging the observations of the infrared objects of interest. An example of infrared ground-based facility is the Very Large Telescope, which is operated by the European Southern Observatory. It composed by four unit telescopes with a mirror of 8.2 m in diameter. Each telescope unit can be operated separately or as an interferometer to reach higher angular resolution. Figure 2.3 displays the ANTU telescope unit of the Very Large Telescope (VLT) used to carry out the near-infrared observations presented in Chapter 5. If near- and mid-infrared observations are feasible from the ground, far-infrared observations are not possible using ground-based telescopes, but can be achieved from space and at altitudes above the water vapour of the Earth's atmosphere with the airborne observatory SOFIA (Stratospheric Observatory for Infrared Astronomy).

Solid-state molecules in ice mantles are identified from *absorption bands* in the near- and mid-infrared, which are associated with vibrational modes of their *functional groups* (Hagen *et al.*, 1980). The latter are specific ensembles of atoms in a molecule, e.g., -OH, -CH$_3$, showing peculiar chemical properties despite of the molecule they are bonded to. Ice mantles in the ISM are predominantly studied in the $\sim 3-16$ μm range through the analysis of the stretching, bending and librational modes (Gibb *et al.*, 2004). Table 2.1 lists the vibrational modes of the solid-state molecules studied in this thesis. The detections of interstellar species in absorption is primarily achieved against infrared continuum sources. Typically used background stars are bright infrared giants (Murakawa *et al.*, 2000; Knez *et al.*, 2005; Boogert *et al.*,

TABLE 2.1: Spectral position of the ice absorption bands studied in this thesis.

Wavelength [λ_{center}]	Vibrational mode	Identification
3.0	O-H stretching	H_2O, CH_3OH
3.53	C-H stretching	CH_3OH
4.67	C-O stretching	CO
6.0	bending	H_2O
6.85	bending	NH_4^+?
9.74	C-O stretching	CH_3OH
13.6	libration	H_2O

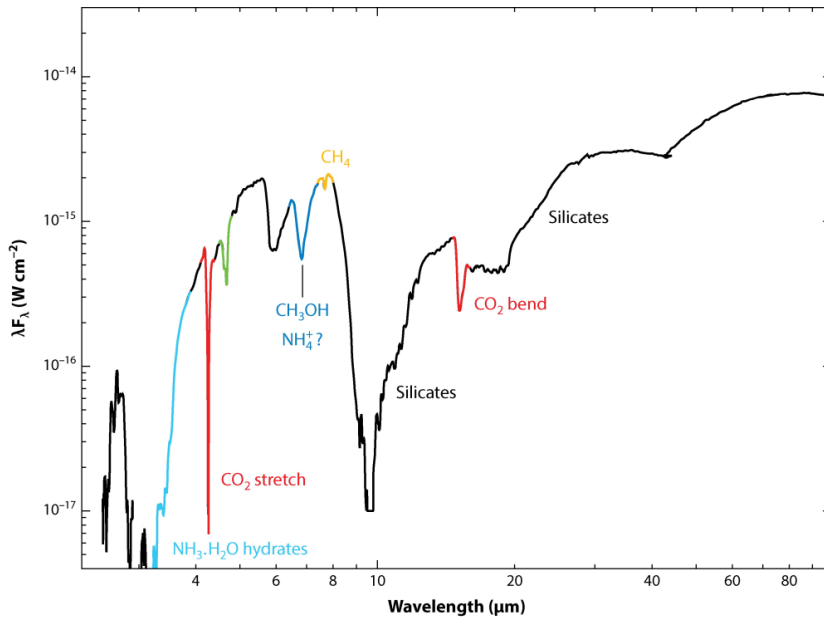**Note:** The values are taken from Boogert *et al.* (2015).

FIGURE 2.4: Near-to-mid infrared spectrum of the massive young stellar object (YSO) AFGL7009 S. The most prominent ice and dust features in this spectral range are indicated. Credit: Boogert *et al.* (2015).

2011; Goto *et al.*, 2020) or Class I young stellar objects (e.g., Pontoppidan *et al.*, 2004; Pontoppidan, 2006; Zasowski *et al.*, 2009; Rocha and Pilling, 2015). Alternatively, the compositions of the ices can be studied in regions where the background emission is enhanced by dust scattering (Pendleton *et al.*, 1990; Honda *et al.*, 2009).

2.2.1 *Decomposition of infrared spectra*

Compared to the ro-vibrational transitions observed in the infrared spectral domain, absorption bands are significantly broader, and therefore not easily attributable to specific functional groups. Figure 2.4 outlines the principal ice and dust features observable at near- and mid-infrared wavelengths, and the molecules primarily responsible for them. Several methods have been developed throughout the years to identify solid-state molecules in infrared spectra. They rely on comparisons with infrared laboratory data. The procedure followed in this thesis to determine to what degree a solid-

state molecule contributes to an observed absorption band consists of initially converting the calibrated infrared spectrum to an optical depth τ scale:

$$\tau = -ln\left(\frac{F_{\text{obs}}}{F_{\text{cont}}}\right) \tag{2.4}$$

where F_{obs} is the observed flux and F_{cont} is the continuum. This is achieved by following the procedure below:

- **Dust continuum determination**
  To accurately determine the continuum, only in specific wavelength ranges (e.g., $\sim 4.5 - 4.9\ \mu$m) it is necessary to remove all the ro-vibrational transitions in the observed spectrum. The resulting spectrum has to include only pure absorption features and the dust continuum. The next step consists of determining the continuum to be used in Eq. 2.4, by fitting a low-order polynomial function to the observed flux spectrum, excluding the regions where ice features are present (Gibb *et al.*, 2004; Boogert *et al.*, 2000; Öberg *et al.*, 2011a). A second option involves the use of Kurucz stellar atmosphere models or black body functions (Pontoppidan *et al.*, 2003b; Pontoppidan *et al.*, 2004). Alternatively, photometry points can be used to produce a reddened spectral energy distribution of the field source, which is then adopted as a local continuum (Boogert *et al.*, 2013).

- **Optical depth calculation**
  After determining the continuum (F_{cont}), the computation of the ratio in Eq. 2.4 generates the optical depth spectrum.

Once the optical depth spectrum is obtained, the spectral decomposition of the observational data is performed, to investigate which solid-state molecules contribute to the observed ice features, and to what extent. The fitting routine adopted in this thesis to carry out the spectral decomposition of the infrared spectra is the open-source Python library OMNIFIT[1] (Suutarinen, 2015a). This code concurrently fits a set of selected laboratory data and analytical functions to the observed infrared absorption features. The OMNIFIT fitting utility operates as follows:

1. The observed infrared spectrum (on an optical depth scale) and the complex refractive index spectrum are imported. The latter contains information on the laboratory data, and in particular on the real and imaginary parts of the complex refractive index, also referred to as the optical constants n and k, as function of wavenumber $\tilde{\nu}$.

2. The complex refractive index spectrum is corrected for grain shape effects, according to the "Continuous Distribution of Ellipsoids" method (Bohren and Huffman, 1983). This treatment is adopted in OMNIFIT to account for the fact that ice analogs reproduced in the laboratory and interstellar ices have different shapes.

3. The fitting parameters are prepared and the fit is performed. If only one laboratory dataset is selected, the parameter will be an initial guess for the best-fit multiplier. Other fitting parameters can be added,

[1] https://ricemunk.github.io/omnifit/

depending on the number of laboratory datasets imported, and kept at a fixed value or allowed to vary during the fit. Additionally, a maximum and minimum value can be specified for each inserted parameter. In this thesis OMNIFIT performs the non-linear optimization using the Levenberg-Marquardt method (Levenberg, 1944; Marquardt, 1963). This consists of fitting the observed spectrum, via an iterative procedure, by finding the parameters for which the sum of the squares of the deviations is at its minimum.

The above steps summarize the OMNIFIT workflow when only one empirical dataset is selected. However, a large set of empirical and analytical data can be fitted simultaneously to the observed infrared spectrum as it is the case for the study presented in Chapter 5. When analytical functions are included in the fit, the resulting fitting parameters will incorporate initial guesses for the position, height and full width at half maximum (FWHM) of the observed absorption band. One of the caveat of OMNIFIT, common to other fitting algorithms adopted in the spectral decomposition of infrared data, is that it finds a local minimum solution, which does not necessarily represent the global minimum. The outcomes of the fit allow to determine whether and to what extent a solid-state species contributes to the observed ice features.

The next sections draw an overview of observations at millimeter wavelengths, used in this thesis to investigate the gas-phase molecular inventory of cold protostellar envelopes.

2.3   OBSERVING MOLECULES AT MILLIMETER WAVELENGTHS

The vast majority of detections in interstellar and circumstellar environments has been achieved in the submillimeter and millimeter spectral domains, predominantly from pure rotational transitions of molecules in their lowest vibrational level and ground electronic state (Williams and Viti, 2013; McGuire, 2018).

The rotational transitions at these wavelength regimes (300 μm–1cm) enable to probe gas emissions from pre-stellar and proto-stellar environments characterized by temperatures below 20 K to the high temperatures of hot-corino regions ($T > 100$ K). Submillimeter and millimeter observations are possible from the ground as Earth's atmosphere is mostly transparent at these wavelengths (Figure 2.2), using one or an array of antennas, i.e., through *single-dish* or *interferometric* observations.

2.3.1   *Single-dish versus interferometric observations*

The minimum angular separation between two resolvable objects in the sky, i.e., the angular resolution of an antenna θ, is related to the wavelength λ and the diameter of the antenna D by (Rayleigh, 1879):

$$\theta \approx \frac{\lambda}{D}. \tag{2.5}$$

The above formula implies that the longer the wavelength of the observations is, the larger the diameter of the antenna has to be to resolve small-scale
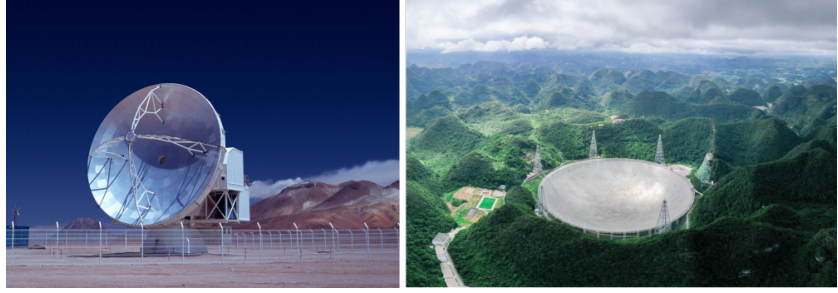
FIGURE 2.5: Examples of single-dishes. *Left:* the Atacama Pathfinder EXperiment (APEX) - Chajnantor plateau, Chile. Credit: ESO. *Right:* the Five-hundred-meter Aperture Spherical radio Telescope (FAST) - Pingtang, China. Credit: Ou Dongqu/Xinhua/ZUMA.

structures in the sky. The existing single-dish telescopes measure from a few tens to a few hundreds of meters. For instance, the Atacama Pathfinder EXperiment (APEX) telescope used in this thesis (Figure 2.5), has a main-dish diameter of 12 m and an angular resolution of $\sim 27''$ at 1.3 mm (Güsten *et al.*, 2006). The world's largest single-dish radio-observatory, the Five-hundred-meter Aperture Spherical radio Telescope (FAST) gets as far as $\sim 100''$ at centimeter wavelengths (Figure 2.5). This angular resolution is excellent to probe the large-scale cloud emission, but it is not sufficient to resolve, e.g., the inner 200 AU of protostellar envelopes, corresponding to sub-arcsecond angular sizes (Schöier *et al.*, 2002) or even smaller structures such as protoplanetary disks (Andrews *et al.*, 2018).

The angular resolution limitation of single dishes can not be overcome by simply constructing larger antennas. Despite being challenging to design from an engineering point of view, such colossal constructions would be troublesome to operate, besides requiring substantial maintenance. Additionally, to an increment in the diameter of the antenna inevitably corresponds a diminution of the surface accuracy of the dish, hampering the achievement of angular resolutions below $10''$ (Rohlfs and Wilson, 1996). Instead, higher angular resolution observations are provided by means of radio-interferometry, which consists of combining the signals collected from multiple separate antennas. The result of this powerful combination is comparable to observing with a huge telescope that has a diameter dictated by the longest distance between a pair of antennas, e.g., a *baseline* D_{int} up to ~ 16 km in the case of the Atacama Large Millimeter/submillimeter Array (ALMA; Figure 2.6). Compared to Eq. 2.5, the angular resolution of an array of antennas is given by:

$$\theta \approx \frac{\lambda}{D_{int}} \qquad (2.6)$$

where D_{int} is the longest baseline of the interferometer. In its most extended 12-m array configuration, ALMA probes the interstellar physical and chemical conditions with an angular resolution of $\sim 0.01''$, which is commensurate to observing nearby star-forming regions down to a few AU.

The highest angular resolution is not required for all science goals. For instance, the observations presented in Chapters 5, 6 and 7 target the outer envelopes of low-mass protostars, and therefore the emission of interstellar molecules over large spatial scales. For this purpose, it is not necessary to make use of the longest baselines of the interferometer, instead, the shortest

FIGURE 2.6: Examples of interferometers. *Left:* the Atacama Large Millimeter/submillimeter Array (ALMA) - Chajnantor plateau, Chile. Credit: ESO. *Right:* the Submillimeter Array (SMA) - Mauna Kea, Hawai'i, USA. Credit: CfA

baselines are most suited. Compared to the longest baselines they recover most of the extended emission and, with respect to single-dish observations they allow to reach angular resolutions sufficiently high $(3 - 4'')$ to resolve compact objects (see Sect. 2.3.4). Figure 2.6 displays the interferometer used to collect the data presented in this thesis, the Submillimeter Array (SMA; Ho *et al.*, 2004). The SMA array is composed by eight 6-m diameter antennas. The shortest baseline in the sub-compact array is 9.5 m, whereas the longest baseline in the very extended configuration is 508 m.

2.3.2 *Two-antenna interferometer*

To describe the basics of interferometry, Figure 2.7 considers for simplicity an interferometer composed by only two antennas. Interferometers constituted by more elements follow the same basic principles. Each antenna receives the radiation from an astronomical source located at an angle θ in the form of plane electromagnetic waves, inducing a signal U. The incoming wave front of the plane wave reaches antennas A_1 and A_2 at different times. This time delay is called *geometric delay* τ_g and it is generated due to the orientation of the baseline described with the vector **b** with respect to the pointing direction of the antennas, i.e., the source position, indicated with the vector **s**:

$$\tau_g = \frac{\mathbf{b} \cdot \mathbf{s}}{c} \tag{2.7}$$

where c is the speed of light. The signals U_1 and U_2 received by each antenna reach the correlator where they are combined (voltage multiplication) and corrected for the time delay (time averaging). The output of this operation is called the *interferometer response* $r(\tau_g)$. The step after the correlation consists of the integration of the interferometer response over time. This operation produces the *sky visibility* $V(u,v)$, where u and v are the coordinates of the plane describing the position of the baseline, i.e., the uv plane. The visibility $V(u,v)$ is defined as the Fourier transform of the specific intensity (or brightness distribution) of the source on the sky $I(x,y)$:

$$V(u,v) = \iint A(x,y)I(x,y)e^{-2\pi i(ux+vy)} \, \mathrm{d}x\mathrm{d}y \tag{2.8}$$

where $A(x,y)$ is the effective collecting area of the antenna. In the equation above, $I(x,y)$ represents the quantity to retrieve from the interferometric observations, the intensity distribution of the astronomical source. If a
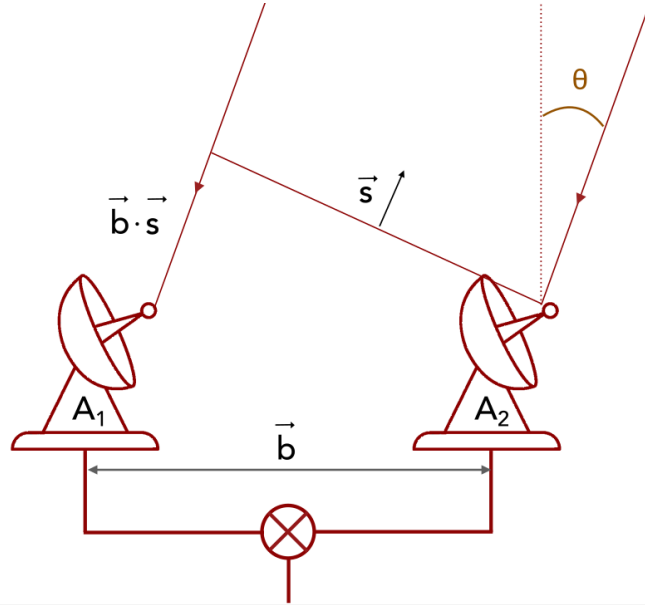
FIGURE 2.7: Schematic illustration of a two-antenna interferometer. Plane waves emitted by an astronomical source reach antennas A_1 and A_2. The source position is indicated by the vector **s**. The orientation of the baseline is described by the vector **b**.

Fourier inversion is applied to Eq. 2.8, the modified specific intensity $I'(x, y)$ is obtained:

$$I'(x, y) = A(x, y)I(x, y) = \iint V(u, v)e^{2\pi i (ux+vy)} \, du dv. \tag{2.9}$$

The two equations above, known as the van Cittert-Zernike theorem (van Cittert, 1934; Zernike, 1938), connect the visibility to the specific intensity of the source. According to the theorem, an image of the intensity of the source can be achieved by inverting the Fourier transform of the visibility. In reality, this is not possible because the antennas do not sample the entire uv plane. To each baseline of the interferometer corresponds one location in the uv plane. In the geometry depicted in Figure 2.7, there is one baseline, which collects one visibility data. Due to Earth's rotation, the position of the u and v coordinates changes with respect to the astronomical source, and this increases the sampling of the uv plane. This concept is represented in Figure 2.8. In an interferometer composed by more elements, even though the antennas are positioned to maximize the coverage of the uv plane, a minimum preventive separation between them is inevitably required, causing a loss of Fourier components during the imaging. Consequently, part of the intensity is unavoidably filtered out, even with the most compact array configurations. To recover part of the "missing" visibilities, in this thesis I combine interferometric and single-dish data following the procedure described in Sect. 2.3.4.

To summarize, throughout each observational run, every baseline collects visibilities, which are integrated over a few tens of seconds. This process is repeated over and over for a number of iterations for all the operative baselines until the coverage of the uv plane is satisfactory or, alternatively, the desired sensitivity is reached. The coverage of the uv plane is highly dependent on the number of operative baselines and on the integration time.
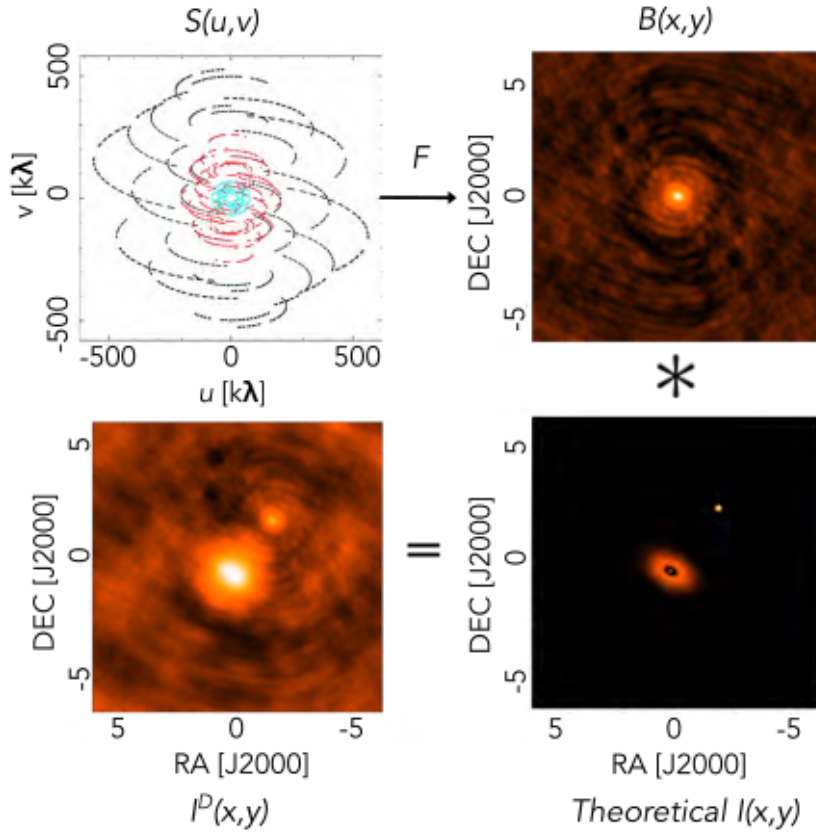
FIGURE 2.8: Relations between the sampling function $S(u, v)$, the dirty beam $B(x, y)$, the intensity distribution $I(x, y)$ and the dirty image $I^D(x, y)$. The Fourier transform of the sampling function is the dirty beam. The dirty image is the result of the convolution of the intensity distribution by the dirty beam. Credit: D. J. Wilner - 2020 SMA Interferometry School.

The higher the number of baselines, the more visibilities will be retrieved and therefore, more information on the intensity of the source will be obtained. Additionally, a longer integration time will result in a better coverage of the uv plane as a consequence of the rotation of the Earth. The totality of the baseline positions in the uv plane acquiring visibility data is defined as the *sampling* function $S(u, v)$. The Fourier transform of $S(u, v)$ is referred to as *dirty beam* $B(x, y)$:

$$B(x, y) = \iint S(u, v)e^{2\pi i(ux+vy)} \, dudv. \qquad (2.10)$$

which represent the response of the interferometer to a point source (point spread function). Figure 2.8 shows an example of sampling function and dirty beam. To a better sampled uv plane (more baselines collecting visibilities) corresponds a more defined dirty beam shape.

To account for the discrepancy in the uv coverage between longer and shorter baselines, the sampled visibility is weighted according to the most appropriate *weighting* function $g(u, v)$. The application of the weighting function is a key step to reduce the imbalance between the longest baselines, which contain information on the small spatial scales, and the shortest baselines, which map the large spatial scales and carry the bulk of the flux. Natural, uniform and Briggs are the most widely used weighting functions. The natural weighting increases the signal-to-noise ratio, at the expense

of the angular resolution. This is because it gives lower weight to the long baselines, whereas the shortest baselines are enhanced. In contrast, the uniform weighting partially attenuates the short baselines, with the inevitable effect of losing some of the recorded flux at larger spatial scales. Often, the Briggs or robust weighting is adopted (Briggs *et al.*, 1999) which allows to achieve a good balance between the uniform and the natural weighting. When a Fourier transform is applied to the sampled visibility, an image of the intensity is obtained:

$$I^D(x, y) = \iint S(u, v)V(u, v)e^{2\pi i(ux+vy)} \tag{2.11}$$

$I^D(x,y)$ is referred to as *dirty image*, and it is related to the dirty beam $B(x, y)$ and the intensity $I(x, y)$ by:

$$I^D(x, y) = I(x, y) * B(x, y), \tag{2.12}$$

the dirty image $I^D(x, y)$ is the convolution ($*$) of the intensity distribution of the source by the dirty beam. Figure 2.8 recapitulates the relations between the sampling function $S(u, v)$, the dirty beam $B(x, y)$, the intensity of the source $I(x, y)$ and the dirty image $I^D(x, y)$. The final image of the intensity distribution of the source of interest is acquired after calibrating the raw data and applying the preferred deconvolution method to erase the effects of the dirty beam from the dirty image.

2.3.3 *Interferometric data calibration and imaging*

Besides carrying the information on the source of interest, the visibilities recorded by the interferometer include "contamination" from atmospheric effects (e.g., atmospheric composition, turbulence, etc.) and from the instrumental effects (e.g., antenna position errors, receiver delays). Therefore, it is necessary to calibrate the visibilities with the outputs of selected calibrators. These are objects (typically quasars, planets, asteroids and satellites) whose positions and fluxes are well-known. Note that each calibration step requires different calibrators with specific characteristics. Each step is summarily described in the following.

1. **Bandpass calibration**
   This calibration step monitors the spectral response to ensure signal at each frequency interval. In particular, it tackles the undesired effects caused by delay offset, cable delays originated in the receiving system, as well as the repercussions due to the presence of molecular oxygen and ozone in the atmosphere. The bandpass calibrators are normally bright point-like sources akin to strong quasars (e.g, 3c84, 3c279), whose spectra are line-free over a few GHz. Quasars are particularly suited for this task as they are strong emitters at all baselines independently on the baseline length.

2. **Phase calibration**
   The second step of the calibration has the objective of removing instrumental and atmospheric phase-variability from the visibilities. Such variability takes place at different timescales in the atmosphere. There

are short-term events mostly associated with atmospheric turbulence akin to variations of water vapour in the atmosphere, and long-term events such long-lasting changes of the weather conditions throughout the observations and antenna position errors.

For the Submillimeter Array datasets, the correction for these fluctuations is carried out by observing gain calibrators. These are usually bright quasars emitting at radio wavelengths. One of the discriminators in the selection of the gain calibrators is their vicinity to the source of interest on the sky. This is because they should ideally cover the same atmospheric properties as the target. This calibration step consists of performing a linear fit or fitting with a spline function the averaged visibilities as function of time.

3. **Amplitude calibration**
   The amplitude calibration is required to eliminate instrumental variability, e.g, sub-optimal antenna pointing and focus, and to apply a residual correction for atmospheric opacity. In general, the amplitude-variability occurs at slower timescales compared to the phase-variability. The amplitude calibration step is similar to the phase calibration, but the amplitude of the visibilities is fitted instead of the phase. Normally, the phase and amplitude calibrations make use of the same calibrators. As the flux of the quasars adopted in the amplitude calibration slightly varies as function of time, their absolute flux is determined by comparison with flux calibrators in the following step.

4. **Flux calibration**
   The final step of the calibration places the visibilities on a consistent flux scale. This process can be compared with the usage of standard stars in optical observations. In this step the antenna temperature (T_A) usually in Kelvin (K) is converted into a flux in Jansky (Jy). The flux calibrators are commonly Solar System sources not heavily resolved by the interferometer such as Uranus, Callisto, and Titan. The selection of the flux calibrator depends on the targeted configuration and angular resolution.

When all the atmospheric and instrumental effects are removed and the observational data are properly calibrated, it is possible to proceed with the imaging to visualize the intensity distribution of the source of interest. The software used in this thesis to both calibrate and image, and more generally to inspect and analyse the interferometric data is the Common Astronomy Software Application (CASA)[2] package (McMullin *et al.*, 2007). The adopted deconvolution method is the CLEAN algorithm (Högbom, 1974), which assumes that the image of the intensity distribution of the source is made of point sources. The clean task constructs a model of the intensity distribution of the source which resembles to the dirty image $I^D(x, y)$. This is achieved through the iterations described below and illustrated in Figure 2.9:

1. Identify the peak in the dirty image $I^D(x, y)$;

2. Subtract a factor γ with the dirty beam shape from the dirty image at the peak position identified in step 1. After the first subtraction, the
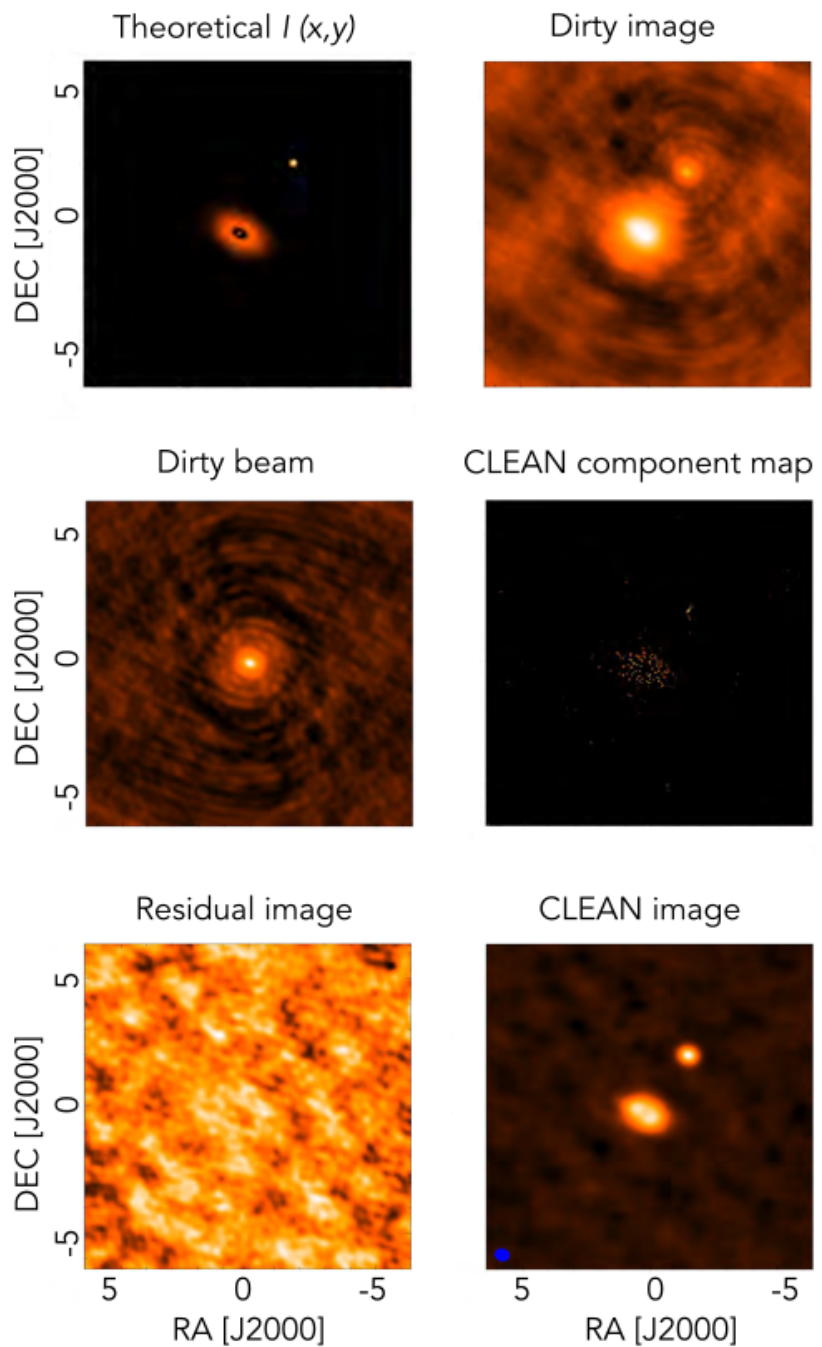
[2] http://casa.nrao.edu/

FIGURE 2.9: Simulation of the CLEAN deconvolution algorithm. The images display the theoretical model of the intensity distribution of the source $I(x, y)$, the dirty image $I^D(x, y)$, the dirty beam $B(x, y)$, the CLEAN component map, the residual image and the restored CLEAN image. Credit: D. J. Wilner - 2020 SMA Interferometry School.

dirty image is referred to as *residual image*. The factor γ is typically ~0.1.

3. Create the *CLEAN component map*, by filling the map with the point sources (i.e., intensity and position values) subtracted from step 2.

4. Iterate steps 1–3 until the peak in the residual image is smaller than a selected stopping threshold, e.g., the peak in the residual image is lower than a fraction of the theoretical rms noise.

Once the above steps are successfully completed, the point sources which are part of the CLEAN component map are convolved with the *CLEAN beam* - which is a Gaussian beam resembling the main lobe of the dirty beam - and added to the residual image (Figure 2.9). The outcome of this last operation is the *CLEAN image* which contains the information of the intensity distribution of the source of interest.

2.3.4 *Combination of interferometric and single-dish data*

When planning an observation, the characteristics of the astronomical source to be observed and the science goals to be addressed are the main factors in the selection of the most suitable radio telescope to use. Interferometers are ideal to study compact objects at high angular resolutions inaccessible with single-dishes, whereas the latter are apt to observe extended objects - since interferometers are unable to fully recover the information on the largest scales (Sect. 2.3.2). However, a number of scientific goals, akin to the projects carried out in Chapters 5, 6 and 7, require high angular resolution observations of extended objects. This implies applying the so called "short-spacing correction" to the interferometric observations, which can be achieved by:

- observing the extended object with the interferometer;

- observing the same object with the single-dish;

- calibrating both datasets to ensure they have analogous flux density scales;

- combining the interferometric and single-dish data using the preferred combination algorithm.

The following provides a description on how interferometric and single-dish data are folded together. A single-dish telescope can be described as sets of small hexagonal panels (Figure 2.10). In this definition the signal received by each hexagon is combined at the center of the dish, commensurate with the combination of the signal coming from individual antennas forming part of an inteferometer. The separation between two hexagonal panels can be referred to as the baseline d, which is equal to zero at the center of the dish. The longest baseline is dictated by the diameter of the single dish D_{sd} (Figure 2.10). This representation makes it possible to interpret a single-dish as an interferometer composed by an infinite number of antennas,
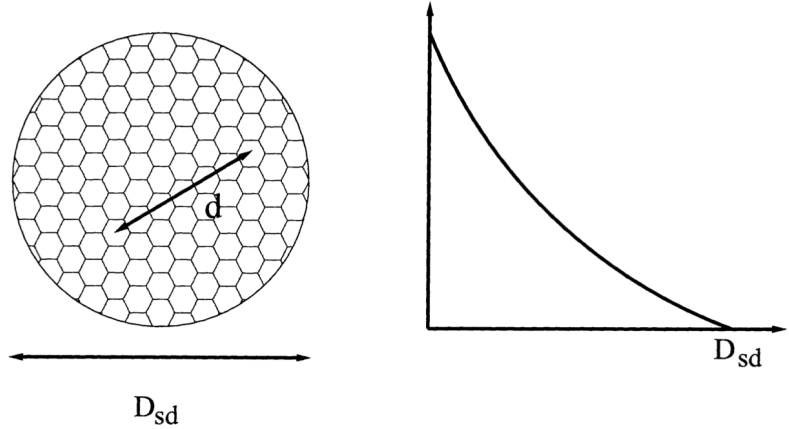
FIGURE 2.10: Schematic illustration of a single-dish represented as an interferometer. *Left:* the hexagonal panels are compared to the antennas composing the interferometer. The separation between the panels is the baseline d and the diameter of the single-dish is D_{sd}. *Right:* Graph illustrating the baseline distribution decreasing from the center of the dish to the longest baseline dictated by D_{sd}. Credit: Stanimirovic (2002)

and by inference to apply the same mathematical notation to single-dish and interferometric data. The *single-dish dirty image* is defined as:

$$I_{sd}^D(x, y) = B_{sd}(x, y) * I(x, y) \qquad (2.13)$$

where $B_{sd}(x, y)$ is the *single-dish dirty beam*. When a Fourier transform is applied to Eq. 2.13, the sampled single-dish visibility $V_{sd}(u, v)$ is obtained. In contrast to the interferometric sampled visibility, $V_{sd}(u, v)$ does not require the application of a weighting function as it is a continuous function. This is due to zero spacing between the hexagonal panels of the single-dish.

The development of techniques to combine single-dish and interferometric data has been pursued since the 80's. Introductions to the subject and to different methods to perform the combination can be found in Vogel *et al.*, 1984; Weiß *et al.*, 2001; Stanimirovic, 2002; Helfer *et al.*, 2003; Kurono *et al.*, 2009; Koda *et al.*, 2011 and references therein. Throughout the years, these techniques have been tested and implemented in the most widely used astronomical data handling packages. The single-dish and interferometric data combined in this thesis employ the `feathering` algorithm, which can be executed in CASA. Figure 2.11 displays the CASA workflow for the combination of interferometric and single-dish data, which is described below:

- **Preparation of the calibrated single-dish image**
  The single-dish image is imported to CASA and it is regridded using the task `imregrid` to match the image shape, the pixel size and the coordinate system of the interferometric image. When this step is completed, the two datasets must have identically gridded spectral axes.

- **Flux conversion of single-dish image**
  Before adding the short-spacing to the interferometric data, both interferometric and single dish images are required to have the same flux density normalization scale. The single-dish image is converted from antenna units to Jy/beam using the `immath` command.
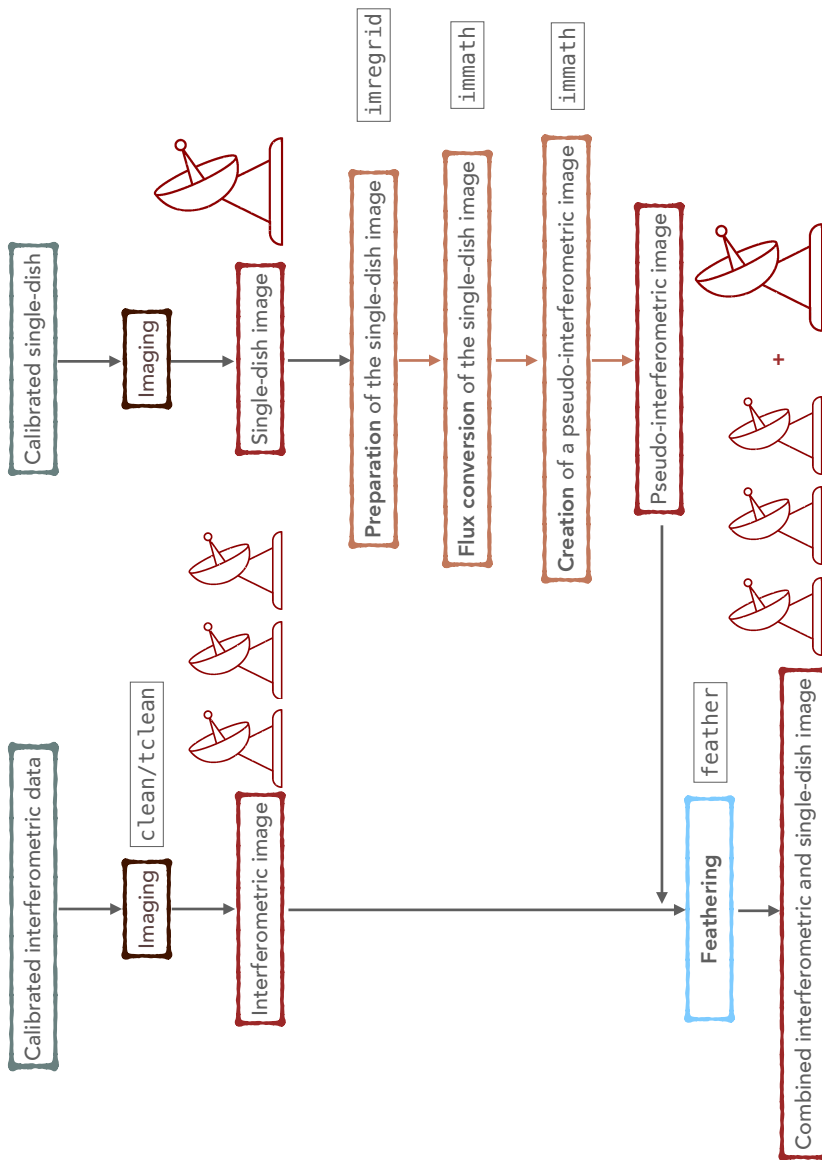
FIGURE 2.11: Workflow describing the step involved in the combination of interferometric and single-dish data.
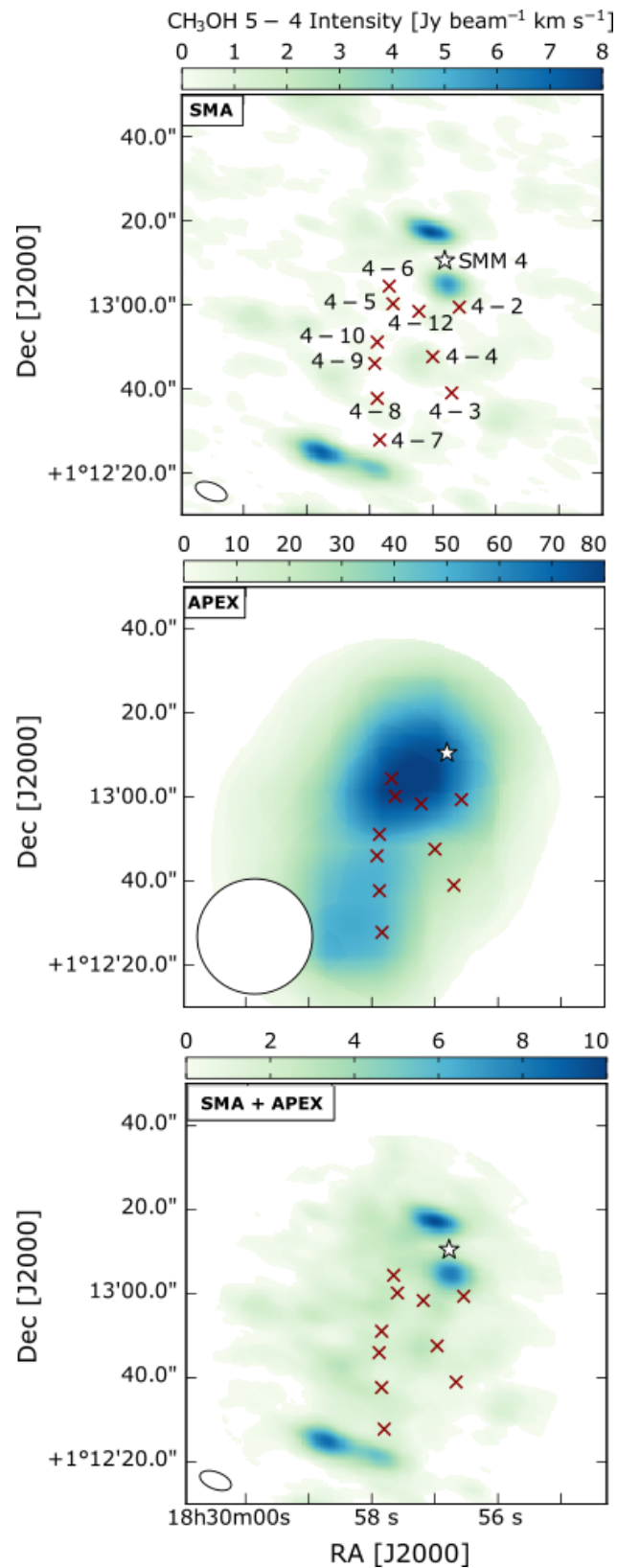
FIGURE 2.12: Example of the combination of interferometric and single dish data. The three panels display integrated intensity maps of the CH_3OH $5 - 4$ A^+ line observed with the SMA (top), the APEX telescope (middle) and the combined SMA + APEX datasets (bottom). The interferometer filters out spatially extended emission. The single-dish telescope retrieves the large-scale emission. The combination of the interferometric and single-dish data recovers the spatially extended emission in the region of interest, where the sources represented by dark red crosses are located.

- **Creation of a pseudo-interferometric image**
  The single-data is multiplied by the interferometric primary beam response to assure that both datasets have the same response on the sky. This step is computed using the `immath` command. The single-dish image is thus transformed into the so-called *pseudo-interferometric* image.

- **Feathering**
  The feathering algorithm is computed using the `feather` command. This task initially scales the intensity of the pseudo-interferometric image by the ratio of the volumes of the interferometric and single dish CLEAN beams. Next, it adds the visibility of the interferometric image to the scaled pseudo-interferometric image in the *uv* plane. The outcome is Fourier-transformed to obtain the combined interferometric and single-dish image. Figure 2.12 displays an example of the combination of interferometric and single-dish using SMA and APEX datasets.

Bibliography

1. ALMA Partnership *et al.*, *ApJ* **808**, L3 (2015).

2. K. Acharyya *et al.*, *A&A* **466**, 1005–1012 (2007).

3. C. M. O. D. Alexander *et al.*, *Geochim. Cosmochim. Acta* **71**, 4380–4403 (2007).

4. V. Allen, M. Cordiner, S. Charnley, *arXiv e-prints* (2020).

5. K. Altwegg *et al.*, *Science Advances* **2**, e1600285–e1600285 (2016).

6. F. O. Alves *et al.*, *ApJ* **904**, L6 (2020).

7. J. Alves, M. Lombardi, C. J. Lada, *A&A* **565**, A18 (2014).

8. S. Andersson, E. F. van Dishoeck, *A&A* **491**, 907–916 (2008).

9. S. Andersson *et al.*, *J. Chem. Phys.* **124**, 064715–064715 (2006).

10. D. P. P. Andrade, M. L. M. Rocco, H. M. Boechat-Roberty, *MNRAS* **409**, 1289–1296 (2010).

11. P. André *et al.*, in *Protostars and Planets VI* (Beuther, Henrik et al., 2014), p. 27.

12. P. André *et al.*, *A&A* **518**, L102 (2010).

13. P. André, *Comptes Rendus Geoscience* **349**, 187–197 (2017).

14. P. Andre, D. Ward-Thompson, M. Barsony, *ApJ* **406**, 122 (1993).

15. S. M. Andrews *et al.*, *ApJ* **869**, L41 (2018).

16. M. Ansdell *et al.*, *AJ* **160**, 248 (Dec. 2020).

17. M. Antiñolo *et al.*, *ApJ* **823**, 25 (2016).

18. E. Artur de la Villarmois *et al.*, *A&A* **626**, A71 (2019).

19. C. R. Arumainayagam *et al.*, *Chemical Society Reviews* **48**, 2293–2314 (2019).

20. Y. Aso *et al.*, *ApJ* **863**, 19 (2018).

21. R. Bachiller *et al.*, *A&A* **295**, L51 (1995).

22. R. Bachiller *et al.*, *A&A* **335**, 266–276 (1998).

23. J. Bally, in *Handbook of Star Forming Regions, Volume I* (Reipurth, B., 2008), vol. 4, p. 459.

24. N. Balucani, C. Ceccarelli, V. Taquet, *MNRAS* **449**, L16–L20 (2015).

25. P. J. Barnes *et al.*, *ApJ* **812**, 6 (2015).

26. D. Barrado *et al.*, *A&A* **526**, A21 (2011).

27. D. Barrado *et al.*, *A&A* **612**, A79 (2018).

28. R. Basalgète *et al.*, *A&A* **647**, A35 (2021).

29. R. Basalgète *et al.*, *A&A* **647**, A36 (2021).

30. M. R. Bate, *MNRAS* **475**, 5618–5658 (2018).

31. A. Bayo *et al.*, *A&A* **536**, A63 (2011).

32. C. P. M. Bell *et al.*, *MNRAS* **434**, 806–831 (2013).

33. C. J. Bennett *et al.*, *ApJ* **660**, 1588–1608 (2007).

34. P. J. Benson, P. C. Myers, *ApJS* **71**, 89 (1989).

35. E. A. Bergin, M. Tafalla, *ARA&A* **45**, 339–396 (2007).

36. J. B. Bergner *et al.*, *ApJ* **841**, 120 (2017).

37. J. B. Bergner *et al.*, *ACS Earth and Space Chemistry* **3**, 1564–1575 (2019).

38. M. Bertin *et al.*, *ApJ* **817**, L12 (2016).

39. E. A. Bibo, P. S. The, D. N. Dawanas, *A&A* **260**, 293–302 (1992).

40. S. E. Bisschop *et al.*, *A&A* **449**, 1297–1309 (2006).

41. L. Bizzocchi *et al.*, *A&A* **569**, A27 (2014).

42. P. Bjerkeli *et al.*, *A&A* **546**, A29 (2012).

43. P. Bjerkeli *et al.*, *A&A* **595**, A39 (2016).

44. R. D. Blandford, D. G. Payne, *MNRAS* **199**, 883–903 (1982).

45. S Blanksby, G Ellison, *Accounts of Chemical Research* **36**, 255–263 (2003).

46. J. Blum, G. Wurm, *ARA&A* **46**, 21–56 (2008).

47. D. Bockelee-Morvan *et al.*, *A&A* **287**, 647–665 (1994).

48. C. F. Bohren, D. R. Huffman, *Absorption and scattering of light by small particles* (New York: Wiley, 1983).

49. A. S. Bolina, W. A. Brown, *Surface Science* **598**, 45–56 (2005).

50. W. B. Bonnor, *ZAp* **39**, 143 (1956).

51. S. Bontemps *et al.*, *A&A* **518**, L85 (2010).

52. A. C. A. Boogert, P. A. Gerakines, D. C. B. Whittet, *ARA&A* **53**, 541–581 (2015).

53. A. C. A. Boogert *et al.*, *A&A* **360**, 683–698 (2000).

54. A. C. A. Boogert *et al.*, *ApJ* **678**, 985–1004 (2008).

55. A. C. A. Boogert *et al.*, *ApJ* **729**, 92 (2011).

56. A. C. A. Boogert *et al.*, *ApJ* **777**, 73 (2013).

57. S. Bottinelli *et al.*, *ApJ* **718**, 1100–1117 (2010).

58. F. Brauer, T. Henning, C. P. Dullemond, *A&A* **487**, L1–L4 (2008).

59. D. Bresnahan *et al.*, *A&A* **615**, A125 (2018).

60. D. S. Briggs, F. R. Schwab, R. A. Sramek, in *Synthesis Imaging in Radio Astronomy II* (Taylor, G. B., Carilli, C. L., and Perley, R. A., 1999), vol. 180, p. 127.

61. T. Y. Brooke, K. Sellgren, T. R. Geballe, *ApJ* **517**, 883–900 (1999).

62. A. Brown, *ApJ* **322**, L31 (1987).

63. V. Buch, R. Czerminski, *J. Chem. Phys.* **95**, 6026–6038 (1991).

64. J. V. Buckle *et al.*, *MNRAS* **399**, 1026–1043 (2009).

65. J. V. Buckle *et al.*, *MNRAS* **422**, 521–541 (2012).

66. J. A. Caballero, *A&A* **478**, 667–674 (2008).

67. H. Calcutt *et al.*, *A&A* **616**, A90 (2018).

68. L. Cambrésy, *A&A* **345**, 965–976 (1999).

69. J. A. Cardelli, G. C. Clayton, J. S. Mathis, *ApJ* **345**, 245 (1989).

70. P. Carlhoff *et al.*, *A&A* **560**, A24 (2013).

71. J. M. Carpenter, *AJ* **120**, 3139–3161 (2000).

72. M. M. Casali, C. Eiroa, W. D. Duncan, *A&A* **275**, 195–200 (1993).

73. S. Cazaux *et al.*, *ApJ* **593**, L51–L55 (2003).

74. S. Cazaux *et al.*, *A&A* **585**, A55 (2016).

75. S. Cazaux *et al.*, *ApJ* **849**, 80 (2017).

76. P. Cazzoletti *et al.*, *A&A* **626**, A11 (2019).

77. C. J. Chandler, J. E. Carlstrom, *ApJ* **466**, 338 (1996).

78. N. L. Chapman *et al.*, *ApJ* **690**, 496–511 (2009).

79. S. B. Charnley, A. G. G. M. Tielens, S. D. Rodgers, *ApJ* **482**, L203–L206 (1997).

80. S. B. Charnley, in *IAU Colloq. 161: Astronomical and Biochemical Origins and the Search for Life in the Universe* (Batalli Cosmovici, Cristiano, Bowyer, Stuart, and Werthimer, Dan, 1997), p. 89.

81. H. Chen *et al.*, *ApJ* **445**, 377 (1995).

82. X. Chen, H. G. Arce, *ApJ* **720**, L169–L173 (2010).

83. J. E. Chiar *et al.*, *ApJ* **426**, 240 (1994).

84. J. E. Chiar *et al.*, *ApJ* **570**, 198–209 (2002).

85. J. E. Chiar *et al.*, *ApJ* **731**, 9 (2011).

86.   M. Choi, *ApJ* **705**, 1730–1734 (2009).

87.   L. E. U. Chu, K. Hodapp, A. Boogert, *ApJ* **904**, 86 (2020).

88.   K. J. Chuang *et al.*, *MNRAS* **455**, 1702–1712 (2016).

89.   K. J. Chuang *et al.*, *MNRAS* **467**, 2552–2565 (2017).

90.   A. Ciaravella *et al.*, *Proceedings of the National Academy of Science* **117**, 16149–16153 (2020).

91.   M. P. Collings *et al.*, *ApJ* **583**, 1058–1062 (2003).

92.   M. P. Collings *et al.*, *MNRAS* **354**, 1133–1140 (2004).

93.   M. S. Connelley, B. Reipurth, A. T. Tokunaga, *AJ* **135**, 2496–2525 (2008).

94.   P. S. Conti, E. M. Leep, *ApJ* **193**, 113–124 (1974).

95.   A. M. Craigon, http://digitool.lib.strath.ac.uk/R/?func=dbin-jump-full&object_id=27550, PhD thesis, Dept. of Physics, Univ. of Strathclyde, 2015.

96.   G. A. Cruz-Diaz *et al.*, *A&A* **592**, A68 (2016).

97.   H. M. Cuppen, E. Herbst, *ApJ* **668**, 294–309 (2007).

98.   H. M. Cuppen *et al.*, *MNRAS* **417**, 2809–2816 (2011).

99.   H. M. Cuppen *et al.*, *Space Sci. Rev.* **212**, 1–58 (2017).

100.   A. Dalgarno, in, ed. by B. Bederson, A. Dalgarno (Academic Press, 1994), vol. 32, pp. 57–68.

101.   T. M. Dame, P. Thaddeus, *ApJ* **297**, 751–765 (1985).

102.   T. M. Dame *et al.*, *ApJ* **322**, 706 (1987).

103.   E. Dartois *et al.*, *A&A* **618**, A173 (2018).

104.   E. Dartois *et al.*, *Astronomy and Astrophysics* **627**, A55 (2019).

105.   E. Dartois *et al.*, *A&A* **634**, A103 (2020).

106.   A. Das *et al.*, *ApJS* **237**, 9 (2018).

107.   C. J. Davis *et al.*, *MNRAS* **309**, 141–152 (1999).

108.   A. Dawes, N. J. Mason, H. J. Fraser, *Phys. Chem. Chem. Phys.* **18**, 1245–1257 (2 2016).

109.   C. H. De Vries, G. Narayanan, R. L. Snell, *ApJ* **577**, 798–825 (2002).

110.   J. T. Dempsey *et al.*, *MNRAS* **430**, 2534–2544 (2013).

111.   J. P. Devlin, *J. Chem. Phys* **96**, 6185–6188 (1992).

112.   J. Di Francesco *et al.*, *ApJS* **175**, 277–295 (2008).

113.   S. Dib, T. Henning, *A&A* **629**, A135 (2019).

114.   O. Dionatos *et al.*, *A&A* **558**, A88 (2013).

115.   O. Dionatos *et al.*, *A&A* **563**, A28 (2014).

116.   C. J. Dolan, R. D. Mathieu, *AJ* **118**, 2409–2423 (1999).

117.   C. J. Dolan, R. D. Mathieu, *AJ* **123**, 387–403 (2002).

118.   B. T. Draine, *ARA&A* **41**, 241–289 (2003).

119.   B. T. Draine, F. Bertoldi, *ApJ* **468**, 269 (1996).

120.   M. N. Drozdovskaya *et al.*, *MNRAS* **490**, 50–79 (2019).

121.   A. Duarte-Cabral *et al.*, *A&A* **519**, A27 (2010).

122.   F. Dulieu *et al.*, *Scientific Reports* **3**, 1338 (2013).

123.   M. M. Dunham *et al.*, in *Protostars and Planets VI* (Beuther, Henrik et al., 2014), p. 195.

124.   M. M. Dunham *et al.*, *ApJS* **220**, 11 (2015).

125.   R. Dupuy *et al.*, *Nature Astronomy* **2**, 796–801 (2018).

126.   A. Duquennoy, M. Mayor, *A&A* **500**, 337–376 (1991).

127.   R. Ebert, *ZAp* **37**, 217 (1955).

128.   P. Ehrenfreund, S. B. Charnley, *ARA&A* **38**, 427–483 (2000).

129.   C. Eiroa, M. M. Casali, *A&A* **223**, L17–L19 (1989).

130. C. Eiroa, A. A. Djupvik, M. M. Casali, in *Handbook of Star Forming Regions, Volume II: The Southern Sky ASP Monograph Publications* (Reipurth, B. ed, 2008), vol. 5, p. 693.

131. C. Eistrup, C. Walsh, E. F. van Dishoeck, *A&A* **595**, A83 (2016).

132. D. D. Eley, E. K. Rideal, *Nature* **146**, 401–402 (1940).

133. I. Evans Neal J. *et al.*, *ApJS* **181**, 321–350 (2009).

134. N. J. Evans II *et al.*, *VizieR Online Data Catalog* **2332** (2014).

135. E. C. Fayolle *et al.*, *ApJ* **739**, L36 (2011).

136. E. C. Fayolle *et al.*, *ApJ* **816**, L28 (2016).

137. G. G. Fazio *et al.*, *ApJS* **154**, 10–17 (2004).

138. G. Fedoseev *et al.*, *MNRAS* **448**, 1288–1297 (2015).

139. G. Fedoseev *et al.*, *MNRAS* **446**, 439–448 (2015).

140. G. Fedoseev *et al.*, *ApJ* **842**, 52 (2017).

141. S. Ferrero *et al.*, *ApJ* **904**, 11 (2020).

142. J. Forbrich, T. Preibisch, *A&A* **475**, 959–972 (2007).

143. J. Forbrich *et al.*, *A&A* **464**, 1003–1013 (2007).

144. D. Foreman-Mackey *et al.*, *PASP* **125**, 306 (2013).

145. H. J. Fraser, E. F. van Dishoeck, *Advances in Space Research* **33**, 14–22 (2004).

146. H. J. Fraser *et al.*, *MNRAS* **327**, 1165–1172 (2001).

147. H. J. Fraser *et al.*, *MNRAS* **353**, 59–68 (2004).

148. S. Frimann, J. K. Jørgensen, T. Haugbølle, *A&A* **587**, A59 (2016).

149. G. W. Fuchs *et al.*, *A&A* **505**, 629–639 (2009).

150. P. A. B. Galli *et al.*, *A&A* **634**, A98 (2020).

151. R. T. Garrod, E. Herbst, *A&A* **457**, 927–936 (2006).

152. R. T. Garrod, V. Wakelam, E. Herbst, *A&A* **467**, 1103–1115 (2007).

153. R. T. Garrod, S. L. Widicus Weaver, E. Herbst, *ApJ* **682**, 283–302 (2008).

154. W. D. Geppert *et al.*, *Faraday Discussions* **133**, 177 (2006).

155. P. A. Gerakines *et al.*, *A&A* **296**, 810 (1995).

156. G. Giardino *et al.*, *A&A* **463**, 275–288 (2007).

157. E. L. Gibb *et al.*, *ApJS* **151**, 35–73 (2004).

158. B. M. Giuliano *et al.*, *A&A* **592**, A81 (2016).

159. P. F. Goldsmith, W. D. Langer, *ApJ* **517**, 209–225 (1999).

160. M. Goto *et al.*, *arXiv e-prints* (2020).

161. R. J. Gould, E. E. Salpeter, *ApJ* **138**, 393 (1963).

162. L. V. Gramajo *et al.*, *AJ* **139**, 2504–2524 (2010).

163. T. Grassi *et al.*, *A&A* **643**, A155 (Nov. 2020).

164. R. O. Gray *et al.*, *AJ* **132**, 161–170 (2006).

165. G. M. Green *et al.*, *ApJ* **810**, 25 (2015).

166. M. J. Griffin *et al.*, *A&A* **518**, L3 (2010).

167. R. J. A. Grim *et al.*, *A&A* **243**, 473 (1991).

168. C. E. Groppi *et al.*, *ApJ* **670**, 489–498 (2007).

169. W. M. Grundy *et al.*, *Science* **367**, aay3705 (2020).

170. R. Güsten *et al.*, *A&A* **454**, L13–L16 (2006).

171. R. A. Gutermuth *et al.*, *ApJ* **673**, L151 (2008).

172. W. Hagen, L. J. Allamandola, J. M. Greenberg, *A&A* **86**, L3–L6 (1980).

173. G. Haro, *ApJ* **115**, 572 (1952).

174. J. Harris, B. Kasemo, *Surface Science* **105**, L281–L287 (1981).

175. D. Harsono *et al.*, *A&A* **562**, A77 (2014).

176. D. Harsono *et al.*, *Nature Astronomy* **2**, 646–651 (2018).

177. P. Hartigan, J. A. Graham, *AJ* **93**, 913 (1987).

178. P. Harvey *et al.*, *ApJ* **663**, 1149–1173 (2007).

179. T. I. Hasegawa, E. Herbst, *MNRAS* **263**, 589 (1993).

180. T. I. Hasegawa, E. Herbst, C. M. Leung, *ApJS* **82**, 167 (1992).

181. T. Hassenkam *et al.*, *Nature* **548**, 78–81 (2017).

182. T. J. Haworth *et al.*, *MNRAS* **501**, 3502–3514 (2021).

183. C. Heiles, H. J. Habing, *A&AS* **14**, 1 (1974).

184. T. T. Helfer *et al.*, *ApJS* **145**, 259–327 (2003).

185. T. Henning, *ARA&A* **48**, 21–46 (2010).

186. T. Henning, G. Meeus, in *Physical Processes in Circumstellar Disks around Young Stars* (Garcia, Paulo J. V., 2011), pp. 114–148.

187. G. H. Herbig, *Vistas in Astronomy* **8**, 109–125 (1966).

188. G. H. Herbig, *ApJ* **111**, 11 (1950).

189. G. H. Herbig, *ApJS* **4**, 337 (1960).

190. E. Herbst, W. Klemperer, *ApJ* **185**, 505–534 (1973).

191. E. Herbst, C. M. Leung, *ApJS* **69**, 271 (1989).

192. E. Herbst, E. F. van Dishoeck, *ARA&A* **47**, 427–480 (2009).

193. G. J. Herczeg *et al.*, *ApJ* **849**, 43 (2017).

194. G. J. Herczeg *et al.*, *ApJ* **878**, 111 (2019).

195. J. Hernández *et al.*, *ApJ* **662**, 1067–1081 (2007).

196. J. Hernández *et al.*, *ApJ* **707**, 705–715 (2009).

197. J. Hernández *et al.*, *ApJ* **794**, 36 (2014).

198. M. Heyer, T. M. Dame, *ARA&A* **53**, 583–629 (2015).

199. C. N. Hinshelwood, in (Oxford University Press, 1940), pp. 36–39.

200. P. T. P. Ho, J. M. Moran, K. Y. Lo, *ApJ* **616**, L1–L6 (2004).

201. S. Hoban *et al.*, *Icarus* **105**, 548–556 (1993).

202. J. A. Högbom, *A&AS* **15**, 417 (1974).

203. D. J. Hollenbach, A. G. G. M. Tielens, *Reviews of Modern Physics* **71**, 173–230 (1999).

204. D. Hollenbach, C. F. McKee, *ApJ* **342**, 306 (1989).

205. D. Hollenbach, E. E. Salpeter, *ApJ* **163**, 155 (1971).

206. M. Honda *et al.*, *ApJ* **690**, L110–L113 (2009).

207. D. M. Hudgins *et al.*, *ApJS* **86**, 713–870 (1993).

208. C. L. H. Hull *et al.*, *ApJ* **847**, 92 (2017).

209. R. L. Hurt, M. Barsony, *ApJ* **460**, L45 (1996).

210. S. Ioppolo *et al.*, *ApJ* **686**, 1474–1479 (2008).

211. S. Ioppolo *et al.*, *MNRAS* **413**, 2281–2287 (2011).

212. S. Ioppolo *et al.*, *A&A* **646**, A172 (2021).

213. M. Ishii *et al.*, *AJ* **124**, 2790–2798 (2002).

214. J. H. Jeans, *Philosophical Transactions of the Royal Society of London Series A* **199**, 1–53 (1902).

215. R. D. Jeffries, *MNRAS* **376**, 1109–1119 (2007).

216. A. Jiménez-Escobar *et al.*, *ApJ* **820**, 25 (2016).

217. A. Jiménez-Escobar *et al.*, *ApJ* **868**, 73 (2018).

218.   I. Jiménez-Serra *et al.*, *A&A* **482**, 549–559 (2008).

219.   I. Jiménez-Serra *et al.*, *Astrobiology* **20**, 1048–1066 (2020).

220.   D. Johnstone *et al.*, *ApJ* **559**, 307–317 (2001).

221.   J. K. Jørgensen *et al.*, *A&A* **415**, 1021–1037 (2004).

222.   J. K. Jørgensen *et al.*, *A&A* **595**, A117 (2016).

223.   J. K. Jørgensen, A. Belloche, R. T. Garrod, *ARA&A* **58**, 727–778 (2020).

224.   G. Jungclaus *et al.*, *Meteoritics* **11**, 231–237 (1976).

225.   J. Kauffmann *et al.*, *A&A* **487**, 993–1017 (2008).

226.   J. V. Keane *et al.*, *A&A* **376**, 254–270 (2001).

227.   M. Keppler *et al.*, *A&A* **617**, A44 (2018).

228.   G. Kim *et al.*, *ApJS* **249**, 33 (2020).

229.   R. F. Knacke *et al.*, *ApJ* **179**, 847–854 (1973).

230.   C. Knez *et al.*, *ApJ* **635**, L145–L148 (2005).

231.   J. Koda *et al.*, *ApJS* **193**, 19 (2011).

232.   K. W. Kolasinski, in (Wiley, J. & Sons Ltd., Chichester, England, 1st Ed., 2002).

233.   V. Könyves *et al.*, *A&A* **584**, A91 (2015).

234.   M. Kounkel, *ApJ* **902**, 122 (2020).

235.   M. Kounkel *et al.*, *AJ* **156**, 84 (2018).

236.   L. E. Kristensen, M. M. Dunham, *A&A* **618**, A158 (2018).

237.   L. E. Kristensen *et al.*, *A&A* **516**, A57 (2010).

238.   M. Kuffmeier, B. Zhao, P. Caselli, *A&A* **639**, A86 (2020).

239.   M. Kuffmeier, T. Haugbølle, Å. Nordlund, *ApJ* **846**, 7 (2017).

240.   Y. Kurono, K.-I. Morita, T. Kamazaki, *PASJ* **61**, 873 (2009).

241.   C. J. Lada, J. H. Black, *ApJ* **203**, L75–L79 (1976).

242.   C. J. Lada, in *Star Forming Regions* (Peimbert, Manuel and Jugaku, Jun, 1987), vol. 115, p. 1.

243.   E. F. Ladd, G. A. Fuller, J. R. Deane, *ApJ* **495**, 871–890 (1998).

244.   W. J. Lang *et al.*, *A&A* **357**, 1001–1012 (2000).

245.   P. Langevin, *J. Phys. Theor. Appl.* **4**, 678 (1905).

246.   I. Langmuir, *Trans. Faraday Soc.* **17**, 607–620 (1922).

247.   B. Larsson *et al.*, *A&A* **363**, 253–268 (2000).

248.   L. Le Roy *et al.*, *A&A* **583**, A1 (2015).

249.   H. H. Lee *et al.*, *A&A* **311**, 690–707 (1996).

250.   H.-T. Lee *et al.*, *ApJ* **624**, 808–820 (2005).

251.   K. I. Lee *et al.*, *ApJ* **797**, 76 (2014).

252.   K. Levenberg, *Quart. Appl. Math.* **2**, 164–168 (1944).

253.   Y. Lin *et al.*, *ApJ* **840**, 22 (2017).

254.   J. E. Lindberg, J. K. Jørgensen, *A&A* **548**, A24 (2012).

255.   J. E. Lindberg *et al.*, *A&A* **584**, A28 (2015).

256.   J. E. Lindberg *et al.*, *A&A* **566**, A74 (2014).

257.   J. E. Lindberg *et al.*, *ApJ* **835**, 3 (2017).

258.   H. Linnartz, S. Ioppolo, G. Fedoseev, *International Reviews in Physical Chemistry* **34**, 205–237 (2015).

259.   T. Liu *et al.*, *ApJS* **222**, 7 (2016).

260.   R. Lüst, A. Schlüter, *ZAp* **38**, 190 (1955).

261.   M.-M. Mac Low, R. S. Klessen, *Reviews of Modern Physics* **76**, 125–194 (2004).

262.   R. J. Maddalena, M. Morris, *ApJ* **323**, 179 (1987).

263. E. E. Mamajek, in *Exoplanets and Disks: Their Formation and Diversity* (Usuda, Tomonori, Tamura, Motohide, and Ishii, Miki, 2009), vol. 1158, pp. 3–10.

264. E. E. Mamajek, M. R. Meyer, J. Liebert, *AJ* **124**, 1670–1694 (2002).

265. S. Manigand *et al.*, *A&A* **635**, A48 (2020).

266. D. Marquardt, *J. Soc. Indust. Appl. Math.* **11**, 431–441 (1963).

267. R. Martín-Doménech, G. M. Muñoz Caro, G. A. Cruz-Díaz, *A&A* **589**, A107 (2016).

268. R. Martín-Doménech *et al.*, *ApJ* **880**, 130 (2019).

269. R. D. Mathieu, in *in Handbook of Star Forming Regions, Volume I. The Northern Sky* (Reipurth, B. ed, 2008), vol. 4, ASP Monographs, p. 757.

270. A. J. Maury *et al.*, *A&A* **621**, A76 (2019).

271. B. A. McGuire, *ApJS* **239**, 17 (2018).

272. J. P. McMullin *et al.*, in *Astronomical Data Analysis Software and Systems XVI* (Shaw, R. A., Hill, F., and Bell, D. J., 2007), vol. 376, p. 127.

273. J. P. McMullin *et al.*, *ApJ* **424**, 222 (1994).

274. J. P. McMullin *et al.*, *ApJ* **536**, 845–856 (2000).

275. S. T. Megeath *et al.*, *AJ* **144**, 192 (2012).

276. S. T. Megeath *et al.*, *AJ* **151**, 5 (2016).

277. C. Meinert *et al.*, *Science* **352**, 208–212 (2016).

278. K. M. Menten *et al.*, *A&A* **474**, 515–520 (2007).

279. D. Mesa *et al.*, *A&A* **624**, A4 (2019).

280. L. Mestel, *MNRAS* **138**, 359 (1968).

281. O. Miettinen *et al.*, *A&A* **486**, 799–806 (2008).

282. M. Minissale *et al.*, *A&A* **585**, A24 (2016).

283. M. Minissale *et al.*, *MNRAS* **458**, 2953–2961 (2016).

284. N. Miyauchi *et al.*, *Chemical Physics Letters* **456**, 27–30 (2008).

285. P. Modica, M. E. Palumbo, G. Strazzulla, *Planet. Space Sci.* **73**, 425–429 (2012).

286. S. J. Mojzsis *et al.*, *Nature* **384**, 55–59 (1996).

287. L. K. Morgan *et al.*, *A&A* **477**, 557–571 (2008).

288. J. C. Mottram *et al.*, *A&A* **600**, A99 (2017).

289. J. Moultaka *et al.*, *A&A* **425**, 529–542 (2004).

290. G. M. Muñoz Caro *et al.*, *ACS Earth and Space Chemistry* **3**, 2138–2157 (2019).

291. H. S. P. Müller *et al.*, *A&A* **370**, L49–L52 (2001).

292. M. J. Mumma, S. B. Charnley, *ARA&A* **49**, 471–524 (2011).

293. K. Murakawa, M. Tamura, T. Nagata, *ApJS* **128**, 603–613 (2000).

294. P. Murdin, M. V. Penston, *MNRAS* **181**, 657 (1977).

295. N. M. Murillo *et al.*, *A&A* **592**, A56 (2016).

296. P. C. Myers, E. F. Ladd, *ApJ* **413**, L47 (1993).

297. P. C. Myers, R. A. Linke, P. J. Benson, *ApJ* **264**, 517–537 (1983).

298. P. C. Myers *et al.*, *ApJ* **324**, 907 (1988).

299. P. C. Myers, *ApJ* **700**, 1609–1625 (2009).

300. F. Nakamura *et al.*, *ApJ* **837**, 154 (2017).

301. J. Nelder, R. Mead, *The Computer Journal* **7**, 308 (1965).

302. D. A. Neufeld, A. Dalgarno, *ApJ* **340**, 869 (1989).

303. R. Neuhäuser, J. Forbrich, in *Handbook of Star Forming Regions, Volume II* (Reipurth, B., 2008), vol. 5, p. 735.

304. R. Neuhäuser *et al.*, *A&AS* **146**, 323–347 (2000).

305. B. Nisini *et al.*, *A&A* **518**, L120 (2010).

306. J. A. Noble *et al.*, *MNRAS* **421**, 768–779 (2012).

307. J. A. Noble *et al.*, *ApJ* **775**, 85 (2013).

308. J. A. Noble *et al.*, *Monthly Notices of the Royal Astronomical Society* **467**, 4753–4762 (2017).

309. J. A. Noble, PhD thesis, Dept. of Physics, Univ. of Strathclyde, 2011.

310. M. Nuevo, G. Cooper, S. A. Sandford, *Nature Communications* **9**, 5276 (2018).

311. D. J. Nutter, D. Ward-Thompson, P. André, *MNRAS* **357**, 975–982 (2005).

312. K. I. Öberg, S. Bottinelli, E. F. van Dishoeck, *A&A* **494**, L13–L16 (2009).

313. K. I. Öberg *et al.*, *ApJ* **621**, L33–L36 (2005).

314. K. I. Öberg *et al.*, *A&A* **504**, 891–913 (2009).

315. K. I. Öberg *et al.*, *ApJ* **740**, 109 (2011).

316. K. I. Öberg, *Chemical Reviews* **116**, 9631–9663 (2016).

317. K. I. Öberg, E. A. Bergin, *Phys. Rep.* **893**, 1–48 (2021).

318. K. I. Öberg, R. Murray-Clay, E. A. Bergin, *ApJ* **743**, L16 (2011).

319. K. I. Öberg *et al.*, *ApJ* **740**, 14 (2011).

320. T. Oka, *Proceedings of the National Academy of Science* **103**, 12235–12242 (2006).

321. G. N. Ortiz-León *et al.*, *ApJ* **869**, L33 (2018).

322. V. Ossenkopf, T. Henning, *A&A* **291**, 943–959 (1994).

323. P. Padoan, Å. Nordlund, *ApJ* **576**, 870–879 (2002).

324. Y. J. Pendleton, A. G. G. M. Tielens, M. W. Werner, *ApJ* **349**, 107 (1990).

325. E. M. Penteado, C. Walsh, H. M. Cuppen, *ApJ* **844**, 71 (2017).

326. G. Perotti *et al.*, *A&A* **643**, A48 (2020).

327. G. Perotti *et al.*, *A&A* **650**, A168 (2021).

328. D. E. Peterson *et al.*, *ApJS* **194**, 43 (2011).

329. H. M. Pickett *et al.*, *J. Quant. Spectr. Rad. Transf.* **60**, 883–890 (1998).

330. J. B. Pickles, D. A. Williams, *Ap&SS* **52**, 443–452 (1977).

331. M. Planck, *Verhandl. Dtsch. phys. Ges.* **2**, 202 (1900).

332. D. Polychroni *et al.*, *ApJ* **777**, L33 (2013).

333. K. M. Pontoppidan, *A&A* **453**, L47–L50 (2006).

334. K. M. Pontoppidan, S. M. Blevins, *Faraday Discussions* **168**, 49–60 (2014).

335. K. M. Pontoppidan, E. F. van Dishoeck, E. Dartois, *A&A* **426**, 925–940 (2004).

336. K. M. Pontoppidan *et al.*, *A&A* **408**, 981–1007 (2003).

337. K. M. Pontoppidan *et al.*, *A&A* **404**, L17–L20 (2003).

338. K. M. Pontoppidan *et al.*, *ApJ* **678**, 1005–1031 (2008).

339. K. M. Pontoppidan *et al.*, in *Protostars and Planets VI* (Beuther, Henrik et al., 2014), p. 363.

340. K. M. Pontoppidan *et al.*, *ApJ* **874**, 92 (2019).

341. M. S. Povich *et al.*, *ApJS* **209**, 31 (2013).

342. T. Preibisch, *A&A* **410**, 951–959 (2003).

343. T. Preibisch, *A&A* **428**, 569–577 (2004).

344. R. E. Pudritz, T. P. Ray, *Frontiers in Astronomy and Space Sciences* **6**, 54 (2019).

345. D. Qasim *et al.*, *A&A* **612**, A83 (2018).

346. D. Qasim *et al.*, *Nature Astronomy* **4**, 781–785 (2020).

347. S.-L. Qin, Y.-F. Wu, *Chinese J. Astron. Astrophys.* **3**, 69–74 (2003).

348. D. Rabli, D. R. Flower, *MNRAS* **406**, 95–101 (2010).

349. F. R. S. Rayleigh, *XXXI. Investigations in optics, with special reference to the spectroscope*, 1879.

350. P. Redondo, C. Barrientos, A. Largo, *ApJ* **836**, 240 (2017).

351.   P. Redondo *et al.*, *A&A* **603**, A139 (2017).

352.   B. Reipurth, *VizieR Online Data Catalog*, V/104 (2000).

353.   B. Reipurth, J. Bally, *ARA&A* **39**, 403–455 (2001).

354.   B. Reipurth, P. Friberg, *MNRAS* **501**, 5938–5947 (2021).

355.   V. M. Rivilla *et al.*, *MNRAS* **483**, L114–L119 (2019).

356.   H. Roberts, T. J. Millar, *A&A* **361**, 388–398 (2000).

357.   T. P. Robitaille, *A&A* **600**, A11 (2017).

358.   T. P. Robitaille *et al.*, *ApJS* **169**, 328–352 (2007).

359.   T. P. Robitaille *et al.*, *ApJS* **167**, 256–285 (2006).

360.   W. R. M. Rocha, S. Pilling, *ApJ* **803**, 18 (2015).

361.   K. Rohlfs, T. L. Wilson, *Tools of Radio Astronomy* (Springer Verlag, 1996).

362.   G. S. Rossano, *AJ* **83**, 234–240 (1978).

363.   L. S. Rothman *et al.*, *Appl. Opt.* **26**, 4058–4097 (1987).

364.   M. Rubin *et al.*, *MNRAS* **489**, 594–607 (2019).

365.   D. P. Ruffle, E. Herbst, *MNRAS* **322**, 770–778 (2001).

366.   D. P. Ruffle, E. Herbst, *MNRAS* **324**, 1054–1062 (2001).

367.   D. Rumble *et al.*, *MNRAS* **448**, 1551–1573 (2015).

368.   M. Sahan, L. M. Haffner, *AJ* **151**, 147 (2016).

369.   G. Santangelo *et al.*, *A&A* **538**, A45 (2012).

370.   S. L. Schnee *et al.*, *ApJ* **634**, 442–450 (2005).

371.   S. Schneider, B. G. Elmegreen, *ApJS* **41**, 87–95 (1979).

372.   F. L. Schöier *et al.*, *A&A* **390**, 1001–1021 (2002).

373.   F. L. Schöier *et al.*, *A&A* **432**, 369–379 (2005).

374.   F. L. Schöier *et al.*, *A&A* **454**, L67–L70 (2006).

375.   W. A. Schutte *et al.*, *A&A* **343**, 966–976 (1999).

376.   D. M. Segura-Cox *et al.*, *ApJ* **866**, 161 (2018).

377.   D. M. Segura-Cox *et al.*, *Nature* **586**, 228–231 (2020).

378.   R. J. Shannon *et al.*, *Nature Chemistry* **5**, 745–749 (2013).

379.   R. J. Shannon *et al.*, *RSC Advances* **4**, 26342–26353 (2014).

380.   S. Sharpless, *ApJS* **4**, 257 (1959).

381.   T. Shimonishi *et al.*, *ApJ* **855**, 27 (2018).

382.   F. H. Shu, *ApJ* **214**, 488–497 (1977).

383.   M. A. J. Simons, T. Lamberts, H. M. Cuppen, *A&A* **634**, A52 (2020).

384.   D. Skouteris *et al.*, *ApJ* **854**, 135 (2018).

385.   M. F. Skrutskie *et al.*, *AJ* **131**, 1163–1183 (2006).

386.   L. Song, J. Kästner, *ApJ* **850**, 118 (2017).

387.   S. Spezzano *et al.*, *A&A* **643**, A60 (2020).

388.   F. Stahler, S. W. Palla, in *The Formation of Stars* (Wiley-VCH Verlag GmbG & Co, 2004).

389.   S. Stanimirovic, in *Single-Dish Radio Astronomy: Techniques and Applications* (Stanimirovic, Snezana et al., 2002), vol. 278, pp. 375–396.

390.   T. P. Stecher, D. A. Williams, *Astrophys. Lett.* **4**, 99 (1969).

391.   D. P. Stevenson, D. O. Schissler, *J. Chem. Phys.* **29**, 282 (1958).

392.   S. E. Strom, G. L. Grasdalen, K. M. Strom, *ApJ* **191**, 111–142 (1974).

393.   K. Sugitani, Y. Fukui, K. Ogura, *ApJS* **77**, 59 (1991).

394.   A. N. Suutarinen *et al.*, *MNRAS* **440**, 1844–1855 (2014).

395. A. Suutarinen, http://oro.open.ac.uk/61309/, PhD thesis, Dept. of Physics, The Open University, 2015.

396. A. Suutarinen, *omnifit v0.1*, https://doi.org/10.5281/zenodo.29354, 2015.

397. K. N. R. Taylor, J. W. V. Storey, *MNRAS* **209**, 5P–10 (1984).

398. S. Terebey, F. H. Shu, P. Cassen, *ApJ* **286**, 529–551 (1984).

399. J. Terwisscha van Scheltinga *et al.*, *A&A* **611**, A35 (2018).

400. W.-F. Thi *et al.*, *A&A* **449**, 251–265 (2006).

401. A. G. G. M. Tielens, W. Hagen, *A&A* **114**, 245–260 (1982).

402. J. J. Tobin *et al.*, *Nature* **492**, 83–85 (2012).

403. J. J. Tobin *et al.*, *ApJ* **805**, 125 (2015).

404. W. Tscharnuter, *A&A* **39**, 207 (1975).

405. B. E. Turner, *ApJ* **501**, 731–748 (1998).

406. Ł. Tychoniec *et al.*, *A&A* **632**, A101 (2019).

407. Ł. Tychoniec *et al.*, *A&A* **640**, A19 (2020).

408. M. Vasta *et al.*, *A&A* **537**, A98 (2012).

409. A. I. Vasyunin, E. Herbst, *ApJ* **769**, 34 (2013).

410. A. I. Vasyunin *et al.*, *ApJ* **842**, 33 (2017).

411. F. Vazart *et al.*, *MNRAS* **499**, 5547–5561 (2020).

412. R. Visser, S. D. Doty, E. F. van Dishoeck, *A&A* **534**, A132 (2011).

413. R. Visser *et al.*, *A&A* **495**, 881–897 (2009).

414. S. N. Vogel *et al.*, *ApJ* **283**, 655–667 (1984).

415. C. M. Wade, *AJ* **62**, 148 (1957).

416. A. F. Wagner, M. M. Graff, *ApJ* **317**, 423 (1987).

417. V. Wakelam *et al.*, *Molecular Astrophysics* **9**, 1–36 (2017).

418. C. Walsh *et al.*, *ApJ* **823**, L10 (2016).

419. F. M. Walter *et al.*, *Mem. Soc. Astron. Italiana* **68**, 1081–1088 (1997).

420. H. Wang *et al.*, *ApJ* **617**, 1191–1203 (2004).

421. N. Watanabe, A. Kouchi, *ApJ* **571**, L173–L176 (2002).

422. Y. Watanabe *et al.*, *ApJ* **745**, 126 (2012).

423. W. D. Watson, E. E. Salpeter, *ApJ* **174**, 321 (1972).

424. W. D. Watson, *ApJ* **183**, L17 (1973).

425. J. C. Weingartner, B. T. Draine, *ApJ* **548**, 296–309 (2001).

426. A. Weiß *et al.*, *A&A* **365**, 571–587 (2001).

427. M. S. Westley *et al.*, *Nature* **373**, 405–407 (1995).

428. G. J. White, M. M. Casali, C. Eiroa, *A&A* **298**, 594 (1995).

429. B. A. Whitney *et al.*, *ApJ* **598**, 1079–1099 (2003).

430. D. C. B. Whittet *et al.*, *ApJ* **742**, 28 (2011).

431. D. A. Williams, S. Viti, *Observational Molecular Astronomy: Exploring the Universe Using Molecular Line Emissions* (Cambridge University Press, 2013).

432. J. P. Williams, W. M. J. Best, *ApJ* **788**, 59 (2014).

433. J. P. Williams, L. A. Cieza, *ARA&A* **49**, 67–117 (2011).

434. T. L. Wilson, *Reports on Progress in Physics* **62**, 143–185 (1999).

435. T. L. Wilson, F. Matteucci, *A&A Rev.* **4**, 1–33 (1992).

436. A. J. Winter *et al.*, *MNRAS* **491**, 903–922 (2020).

437. M. G. Wolfire, D. Hollenbach, A. G. G. M. Tielens, *ApJ* **344**, 770 (1989).

438. E. L. Wright *et al.*, *AJ* **140**, 1868–1881 (2010).

439. B. Yang *et al.*, *ApJ* **718**, 1062–1069 (2010).

440. H.-W. Yi *et al.*, *ApJS* **236**, 51 (2018).

441. H.-W. Yi *et al.*, *arXiv e-prints*, arXiv:2103.03499 (2021).

442. L. Zamirri *et al.*, *MNRAS* **480**, 1427–1444 (2018).

443. G. Zasowski *et al.*, *ApJ* **694**, 459–478 (2009).

444. F. Zernike, *Physica* **5**, 785–795 (1938).

445. C. Y. Zhang *et al.*, *A&A* **218**, 231–240 (1989).

446. C. Zhang *et al.*, *MNRAS* **497**, 793–808 (2020).

447. Z.-Y. Zhang *et al.*, *Nature* **558**, 260–263 (2018).

448. C. Zucker *et al.*, *ApJ* **879**, 125 (2019).

449. C. Zucker *et al.*, *A&A* **633**, A51 (2020).

450. P. H. van Cittert, *Physica* **1**, 201–210 (1934).

451. E. F. van Dishoeck, in *Millimetre and Submillimetre Astronomy* (Wolstencroft, R. D. and Burton, W. B., 1988), vol. 147, p. 117.

452. E. F. van Dishoeck, J. H. Black, *ApJS* **62**, 109 (1986).

453. E. F. van Dishoeck, E. A. Bergin, *arXiv e-prints* (2020).

454. E. F. van Dishoeck, J. H. Black, *ApJ* **334**, 771 (1988).

455. E. F. van Dishoeck, G. A. Blake, *ARA&A* **36**, 317–368 (1998).

456. M. L. van Gelder *et al.*, *A&A* **639**, A87 (2020).

457. S. E. van Terwisga *et al.*, *A&A* **640**, A27 (2020).

458. H. C. van de Hulst, *Recherches Astronomiques de l'Observatoire d'Utrecht* **11**, 2.i–2 (1946).

459. M. L. R. van 't Hoff *et al.*, *A&A* **599**, A101 (2017).

460. M. L. R. van 't Hoff *et al.*, *ApJ* **864**, L23 (2018).